Size-Induced Chemical and Magnetic Ordering in Individual Fe–Au Nanoparticles

Pinaki Mukherjee,[†,‡,*] Priyanka Manchanda,[‡,§,∥] Pankaj Kumar,[∥] Lin Zhou,[⊥] Matthew J. Kramer,[⊥] Arti Kashyap,[∥] Ralph Skomski,[‡,§] David Sellmyer,[‡,§] and Jeffrey E. Shield[†,‡,*]

[†]Department of Mechanical & Materials Engineering, [‡]Nebraska Center for Materials and Nanoscience, and [§]Department of Physics & Astronomy, University of Nebraska, Lincoln, Nebraska 68588, United States, [∥]School of Basic Sciences, Indian Institute of Technology Mandi, HP 175001, India, and [⊥]Materials Sciences and Engineering Division, Ames Laboratory, Iowa State University, Ames, Iowa 50011, United States

ABSTRACT Formation of chemically ordered compounds of Fe and Au is inhibited in bulk materials due to their limited mutual solubility. However, here we report the formation of chemically ordered $L1_2$-type Fe_3Au and $FeAu_3$ compounds in Fe–Au sub-10 nm nanoparticles, suggesting that they are equilibrium structures in size-constrained systems. The stability of these $L1_2$-ordered Fe_3Au and $FeAu_3$ compounds along with a previously discovered $L1_0$-ordered FeAu has been explained by a size-dependent equilibrium thermodynamic model. Furthermore, the spin ordering of these three compounds has been computed using *ab initio* first-principle calculations. All ordered compounds exhibit a substantial magnetization at room temperature. The Fe_3Au had a high saturation magnetization of about 143.6 emu/g with a ferromagnetic spin structure. The $FeAu_3$ nanoparticles displayed a low saturation magnetization of about 11 emu/g. This suggests a antiferromagnetic spin structure, with the net magnetization arising from uncompensated surface spins. First-principle calculations using the Vienna *ab initio* simulation package (VASP) indicate that ferromagnetic ordering is energetically most stable in Fe_3Au, while antiferromagnetic order is predicted in FeAu and $FeAu_3$, consistent with the experimental results.

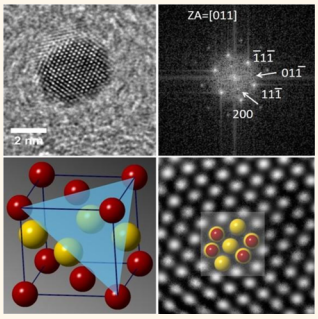

KEYWORDS: chemical ordering · nanoparticles · Fe–Au · nanomagnetism · thermodynamics

Nanoscale structures, and in particular nanoparticles and other size-constrained systems, continue to be an avenue for accessing structures and phases not observed in commensurate equilibrium or near-equilibrium systems.[1,2] The differing thermodynamics and kinetics in nanoparticles provide an opportunity to explore new phases and phase equilibria and to discover new materials with unique catalytic, magnetic, or optical properties[3−5] for use in a variety of applications. Among the nonequilibrium phenomena observed in metallic particles are the formation of nonequilibrium atomic structures,[6] extension of solid solubility[7] and mixing of immiscible elements,[8,9] and suppression of phase transitions.[2,10,11] The key aspect missing in these works is finding the most stable thermodynamic state of the system, which is usually achieved, experimentally, by heat treatment followed by slow (furnace) cooling. The equilibrium stabilization of a phase or structure is confirmed if the structure is favored energetically, and subsequently, the laws of thermodynamics can be invoked to calculate the energetics of the phase stabilization driven by size. The Fe–Au bimetallic system, as a case study, provides an excellent opportunity to study the size-driven stabilization of the thermodynamic phases because of its contrasting phase-behavior in bulk and nanostructures. In the equilibrium Fe–Au system,[12] due to limited solubility and positive heat of mixin,g[13] slow cooling results in phase separation for a wide range of composition. Recently, in the Fe–Au nanoparticles, a critical radius-of-transition, which describes the onset of phase-separation (into bulk phases), has been discovered,[14] and similar behavior has been observed in other systems as well.[15] Single-phase solid solutions are stabilized below the critical radius, and phase separation occurs above it. Subsequently, we have discovered chemical ordering within these nanoscale solid solutions, at specific atomic ratios (1:2, 1:1[16] and 2:1). In

* Address correspondence to pmukherjee@unl.edu, jshield@unl.edu.

Received for review April 21, 2014 and accepted July 10, 2014.

Published online July 10, 2014
10.1021/nn5022007

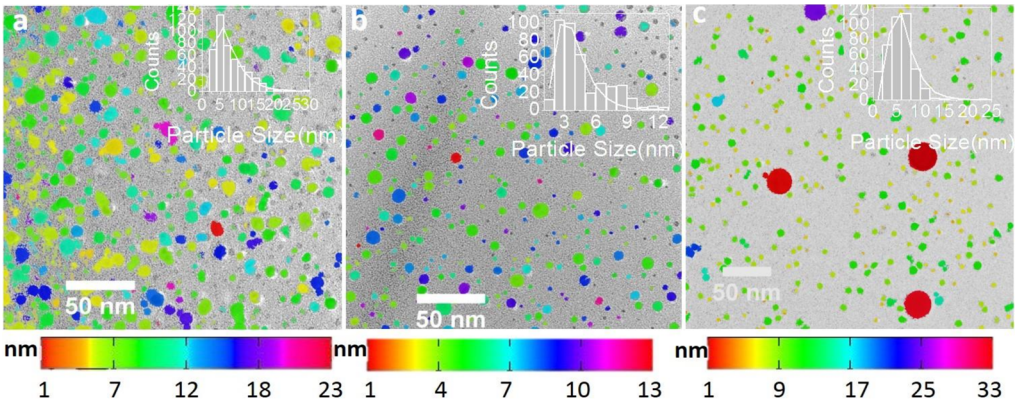

Figure 1. Size distribution of Fe−Au nanoparticles: TEM bright-field micrograph of Fe−Au particles deposited on a carbon substrate. The color map superimposed on the actual image shows size distribution of annealed nanoparticles. a, b, c represent 79, 53, and 33 atom % Fe, respectively. (Insets) Histogram with a log-normal fit of the particle size distribution.

this work, we focus on the formation and stabilization (through annealing) of chemically ordered structures in the Fe−Au nanoparticles at 1:2 and 2:1 stoichiometries with an average size below 10 nm. The stability of these nanocompounds has been explained using a size-dependent thermodynamic model and the magnetic behavior measured and predicted using first-principle calculations.

Modifying the atomic (or chemical) ordering in a unit cell provides a means to further control or alter a material's properties.[17,18] This can be observed in many chemically ordered structures in transition-metal compounds, which are especially prevalent between 3d and noble metals, with the most common structure types being $L1_2$ and $L1_0$. For example, alloying ferromagnetic Fe or Co with the exchange-enhanced Pauli paramagnets Pt and Pd yields the highly anisotropic ferromagnetic and chemically ordered compounds FePt, FePd, and CoPt,[19−21] whereas $FePt_3$ and FeRh are antiferromagnetic.[22,23] Recently, Au-rich chemically synthesized nanoparticles have reportedly formed the $L1_2$ Au_3Fe structure,[24,25] and gas-condensed FeAu nanoparticles formed in the $L1_0$ structure.[16] The Au_3Fe was reported to be superparamagnetic with a low magnetization at room temperature,[24] while FeAu was ferromagnetic with low magnetization.[16] No further information about magnetic behavior of these ordered structures is provided in these works. In the current research, the stabilization of the nonequilibrium Fe−Au $L1_2$ and $L1_0$ phases indicates toward a new set of size-driven spin structures in confined nanosized systems, with no such structural/magnetic phases being present in their bulk counterparts. For the first time, magnetic ordering and spin structures of the newly formed structures are reported from both theoretical (first-principle calculations) and experimental perspectives.

RESULTS AND DISCUSSION

We have investigated three nanoparticle samples with different atomic percentages of Fe, labeled 2P (79 atomic percent Fe), 6P (53 atomic percent Fe), and 8P (33 atomic percent Fe), where "P" refers to number of Au plugs in the Fe target. These compositions are relatively close to those predicted from the sputtering rates and relative area fractions of Au and Fe on the target. The compositions of the annealed particles remain unchanged within experimental error. The as-deposited particles are either bcc (2P) or fcc (6P and 8P). Complete characterization of the as-deposited particles is reported elsewhere.[7] Here, we focus on structures formed during heat treatment. The heat-treated particles were of uniform size, as indicated by TEM images, although some agglomeration (sintering) of particles in contact with one another did occur during heat treatment. Figure 1 shows the particle-size distribution for each composition. The distribution follows a log-normal function which takes into account asymmetry introduced by the agglomerates.[26] The average particle size was determined to be 7.9 ± 4.4, 4.7 ± 2.4, and 5.8 ± 3.5 nm for the samples 2P, 6P, and 8P, respectively.

The structures formed in the particles after heat treatment were determined using fast Fourier transforms (FFTs) of the high-resolution TEM images as well as selected area electron diffraction (SAED). The high-resolution images revealed that the particles are single crystalline and highly ordered (Figures 2a and 3a). This is confirmed by the sharp diffraction maxima in (Figures 2d and 3a), with minimal defects present. For sample 2P (Figure 2), which contains 79 atom % Fe, the FFT reveals a pattern of intense reflections characteristic of the [011] zone axis for an fcc structure. However, closer inspection reveals a set of weak reflections midway between the {200} and {220} reflections which correspond to the {100} and {110} superlattice reflections of a $L1_2$-type ordered structure with a lattice parameter of 0.365 nm. The composition of these particles is 20 atomic percent Au, close to the required Fe_3Au stoichiometry necessary for $L1_2$ ordering. The SAED pattern reveal {110} and {211} superlattice reflections, suggesting $L1_2$-type ordering, while the

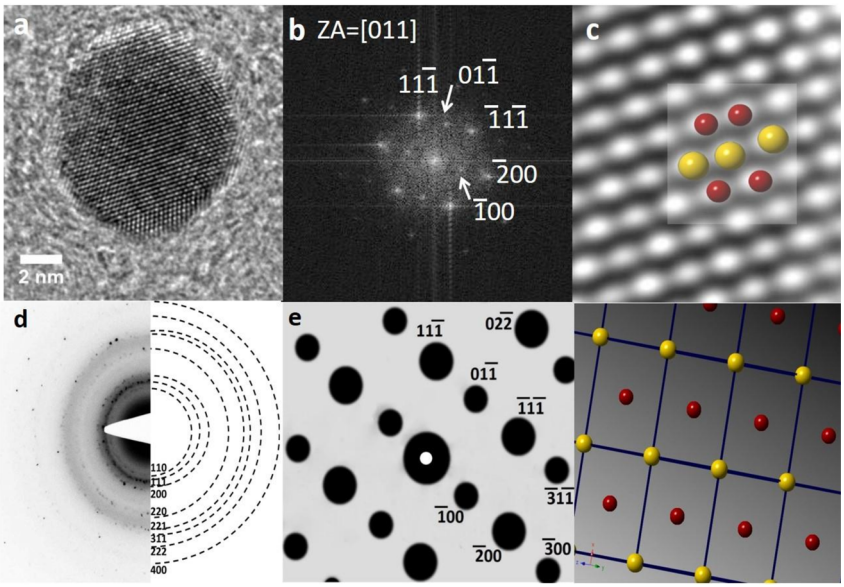

Figure 2. Structural analysis of Fe_3Au ($L1_2$) phase: (a) HRTEM image of a particle. (b, e) Experimental and simulated fast Fourier transform of the HRTEM image, which indexes to the [011] zone axis of a ordered $L1_2$ structure. (d) The SAED pattern was indexed to $L1_2$ structure with a lattice parameter a = 0.365 nm. (c) A magnified and background refined view of (a) with an overlay of the unit cell projection along [011] zone axis. (f) Simulated projection of $L1_2$ structure along the [011] zone axis. Red and yellow spheres show Fe and Au atoms, respectively.

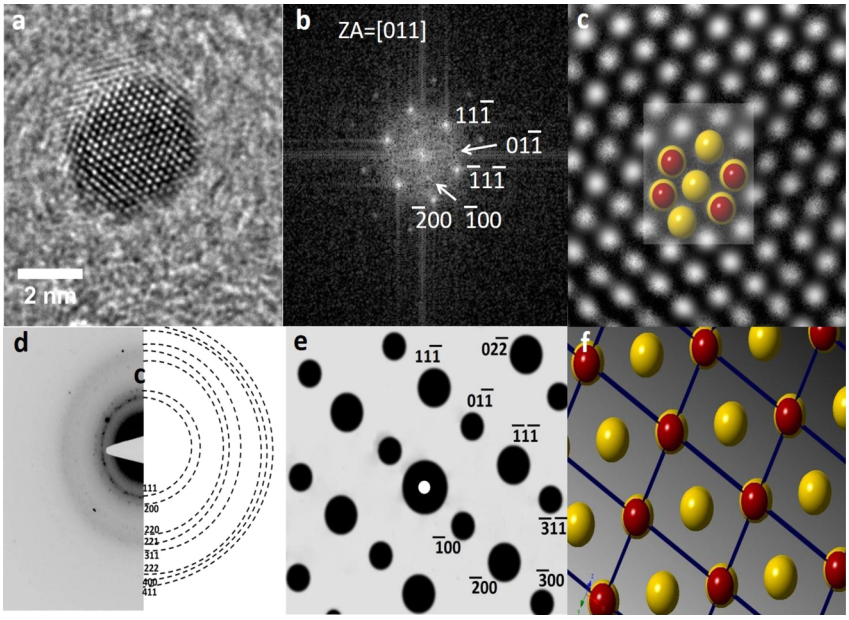

Figure 3. Structural analysis of $FeAu_3$ ($L1_2$) phase: (a) HRTEM image of a particle. (b, e) Experimental and simulated fast Fourier transform of the HRTEM image, which indexes to the [011]zone axis of a ordered $L1_2$ structure d. The SAED pattern was indexed to the $L1_2$ structure with a lattice parameter a = 0.371 nm. (c) A magnified and background refined view of (a) with an overlay of the unit cell projection along [011] zone axis. (f) Simulated projection of $L1_2$ structure along the [011] zone axis. Red and yellow spheres show Fe and Au atoms, respectively.

lattice parameter determined from the FFT was corroborated.

For sample 6P, which contains 53 atom % Fe (a composition close to the 1:1 stoichiometry) the structure is determined to be tetragonal with $c = 0.360 \pm 0.010$ nm and $a = 0.374 \pm 0.003$ nm. The details about this structure is presented in the Supporting Information. Additionally, a more complete analysis would be found elsewhere.[16]

For sample 8P, which contains 33 atom % Fe, the FFT in Figure 3b again shows weak {110} and {100} superlattice reflections indicative of structural ordering. This FFT was indexed to the [011] zone axis. The structure was determined to be the $L1_2$ structure with a lattice parameter of 0.371 nm. The SAED pattern here was consistent with the $L1_2$ structure rather than other possible ordered structures such as the

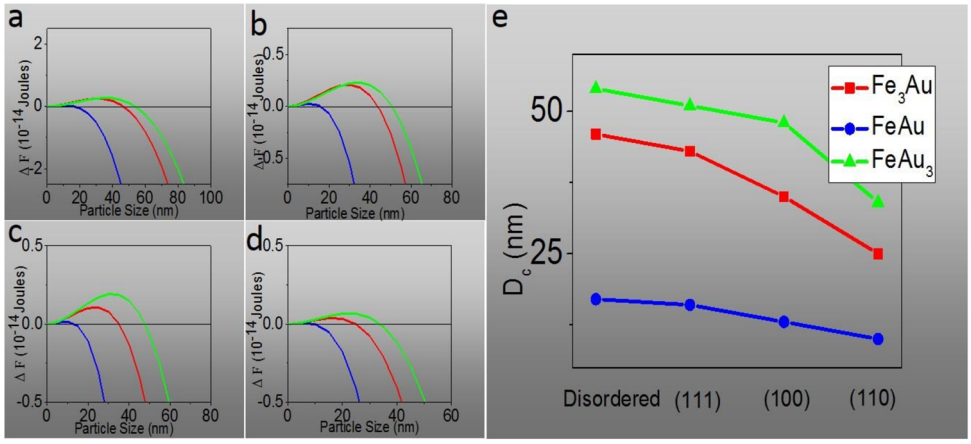

Figure 4. Energetics of nanocompound formation: Stability factor (ΔF) for three nanocompounds $L1_2$ Fe_3Au, Au_3Fe, and $L1_0$ FeAu. A positive value of ΔF indicates that the heat of formation of these nanocompounds is less than their surface energy for certain size range. ΔF is calculated using four different kinds of surfaces: (a) disordered, (b) {111}, (c) {100}, and (d) {110}. (e) The critical diameter of transition D_T, below which nanocompounds are stable are shown for these four kinds of surfaces. From disordered to (110) surfaces the total surface energy of nanoparticles deceases steadily and as a consequence the D_T decreases also.

tetragonal $L6_0$, indicated by the presence of the {221} and {411} rings.

The formation of ordered structures in the Fe−Au system is surprising given the positive heat of mixing (HOM) in this system, which indicates that Fe−Fe and Au−Au bonds are preferable over Fe−Au bonds and results in the phase separation reflected in the equilibrium phase diagram. However, previous work reported that nanoscale system sizes effectively suppressed equilibrium phase behavior.[27] The stabilization of compounds or phases in nanoparticles arises from a competition between the HOM and the total surface energy $(SE)_{tot}$ of the nanoparticle and the interphase interfaces created.[14,27] The HOM is a size-dependent physical property, and with a reduction in system size the HOM decreases, resulting in increasing miscibility between the two constituents (in this case, Fe and Au). The size-dependent HOM can be expressed as[28]

$$\frac{H_m(D)}{H_{mb}} = \exp\left(-\frac{2S_{mb}}{3R}\frac{1}{\frac{D}{D_c}-1}\right)\left(1-\frac{1}{\frac{D}{D_c}-1}\right) \quad (1)$$

where $H_m(D)$ and H_{mb} represent the size-dependent and bulk HOM, respectively. D is the particle diameter and D_c is the critical diameter, which is usually determined to be half of the bond length of A−B type bonds. S_{mb} is the bulk entropy of mixing and is given by

$$S_{mb} = -R(x_A \ln x_A + x_B \ln x_B) \quad (2)$$

where x_A and x_B are the mole fractions of component A and B, respectively.

The total SE of the nanoparticle $(SE)_{tot}$ is the surface energy per unit area $(SE)_A$ multiplied by the surface area of the nanoparticle. The $(SE)_A$ is determined by the composition of the nanocompounds and atomic arrangement of the relevant crystallographic surface. The $(SE)_{tot}$ decreases with size because the surface area decreases with particle diameter. However, the decrease in HOM is an exponential function of particle size D, and decreases more rapidly than the $(SE)_{tot}$, which is proportional to the square of the particle size D. The model excludes edge effects and the size dependence of the $(SE)_A$ is not considered. Thus, at small particle sizes a system that normally prefers atomic clustering or segregation due to a positive HOM can instead form an ordered compound because the surface energy is minimized in an ordered structure while the HOM is decreased.

The transition point (critical size) where ordered compounds are energetically favored compared to the HOM can be quantified by comparing the changes in HOM due to size with the effects of different surface configurations on the total surface energy (see the Supporting Information for details of the calculations). To accomplish this, a stability factor ΔF can now be introduced; this is simply the difference between the total surface energy of a nanoparticle $(SE)_{tot}$ and the size-dependent HOM $H_m(D)$. When ΔF is negative, $H_m(D)$ is larger and atomic clustering/segregation is preferred. When ΔF is positive, nanocompound formation (*i.e.*, chemical ordering) can occur. Here, four different kinds of surfaces were considered for each of the three nanocompounds: chemically disordered and ordered {111}, {110}, and {100} surfaces (Figure 4a−d). The values of the bulk HOM and elemental surface energies were obtained from refs 29 and30, respectively. Figure 4a−d shows the critical nanoparticle diameters D_T (the size at which ΔF changes sign) below which an ordered structure can form. The lowest values of D_T are obtained for {110} surfaces. For this surface configuration, the $L1_2$-ordered $FeAu_3$ and Fe_3Au are stable below 34 and 25 nm, respectively.

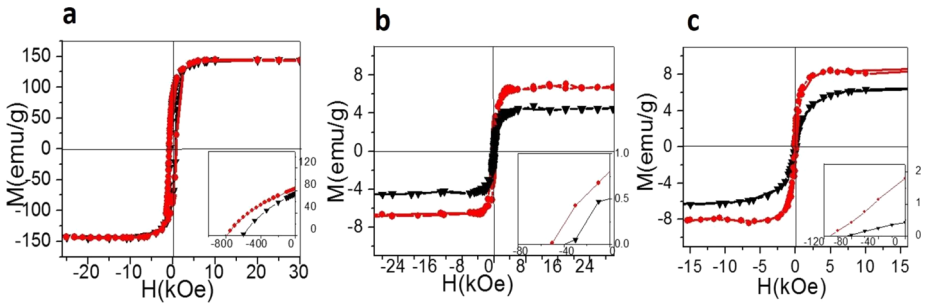

Figure 5. Magnetization (M) Vs. Applied field (H) loops of Au−Fe nanoparticles at 10 and 300 K: (a, b, c) compositions 79, 53, and 33 atom % Fe, respectively. The properties at 10 and 300 K are represented by red dots and black triangles, respectively. The insets show second quadrant behavior.

The $L1_0$-ordered FeAu is stable below 10 nm. The nanoparticles investigated in this study were all below these critical sizes. There is a steady decrease in D_T when the nanoparticle surface changes from disordered → {111} → {100} → {110} as the surface energy of the nanoparticles $(SE)_{tot}$ decreases through this sequence. There are some reports[31,32] of an increase in $(SE)_A$ with deceasing particle size, which would increase the critical size. The surface energies calculated here represent approximate values, as the necessary parameters such as heat of atomization and melting temperature for calculating the surface energies of these newly discovered compounds are not known. However, we used our method of approximating surface energies for systems with known surface energies (NiAl, Ni_3Al, FePt, and CoPt).[33,34] Our approximate values are within 15%, and usually much closer, of the reported values for these compounds. Thus, the approximate surface energies used in our models for these new Fe−Au compounds are reasonable. The stabilization of nanocompounds as a consequence between surface energy and heat of formation is similar to the stabilization of solid-solution phases in finite-sized systems arising from an inability of the system to accommodate an interphase interface.[14]

Figure 5 shows the magnetization behavior for the three ordered structures. The saturation magnetization for FeAu and $FeAu_3$ are very low, corresponding to 0.23 and 0.51μ_B per Fe atom, respectively. Fe_3Au, on the other hand, was observed to have a significant magnetization with a magnetic moment per Fe atom close to bulk Fe values (Table 1). The low magnetization of the FeAu and $FeAu_3$ can be explained by the presence of antiferromagnetic order, with the low magnetization values arising from uncompensated surface spins.[35] Approximating the number of surface Fe atoms and assuming that they all have a magnetic moment close to the surface value of 2.84μ_B[36] results in a saturation magnetization close to the experimentally observed value (Table 1). Thus, it is reasonable to assume AFM ordering in FeAu and $FeAu_3$. The presence of a ferromagnetically ordered structure with a high magnetization in Fe_3Au may make this structure useful in a number of applications, particularly in biomedical applications.

TABLE 1. Magnetic Properties of Ordered Nanoparticles[a]

		M_S (emu/g)		coercivity (Oe)		moment/Fe atom (μ_B)	
ordering type	particle size (nm)	10 K	300 K	10 K	300 K	expt 10 K	theory 0 K
Fe_3Au	7.9 ± 4.4	143.62	142.5	790	580	2.98	2.49
FeAu	4.7 ± 2.4	9	6	52	39	0.23	0
$FeAu_3$	5.8 ± 3.5	11	9	90	50	0.85	0.51

[a] Net moments per Fe atom were deduced from the saturation magnetization M_S (mass polarization) of the nanoparticles.

All three ordered structures displayed low coercivity, including the tetragonal $L1_0$ structure (FeAu). However, in the case of FeAu, the anisotropy may be sufficiently high to prevent magnetization switching in a field of 70 kOe [7 T], particularly if the magnetization is rather low.

The magnetic ordering of Fe−Au compounds was studied theoretically in bulk and nanoparticle configurations. The stable magnetic configurations of $L1_2$ Fe_3Au and $FeAu_3$, and $L1_0$ FeAu in bulk were determined using first-principles calculations. The magnetic ordering has been calculated by comparing the energy difference of ferromagnetic and antiferromagnetic configurations. For the $L1_2$-ordered Fe_3Au, the ferromagnetic configuration was determined to be more stable, consistent with experimental observations. For $L1_2$-ordered Au_3Fe, the antiferromagnetic configuration was calculated to have lower energy, again consistent with the experimental explanation of the low magnetization value. For $L1_0$-ordered FeAu, the ferromagnetic configuration is slightly more favorable than the antiferromagnetic (AFM) configuration, but the calculated energy difference is very small, about 3.5 meV/unitcell, and small perturbations may be sufficient to stabilize an AFM structure.

Modeling of small, 43 atom clusters was utilized to determine the magnetic moments carried by each kind of atom. The compositions of the model particles are $Fe_{36}Au_7$, $Au_{31}Fe_{12}$, and $Fe_{24}Au_{19}$, which correspond to $L1_2$−Fe_3Au, $L1_2$−Au_3Fe, and $L1_0$−FeAu, respectively. Figure 6 shows the atomic arrangements of these clusters. The calculated magnetic moments for Au atoms were of the order of 0.05μ_B; as a result, the

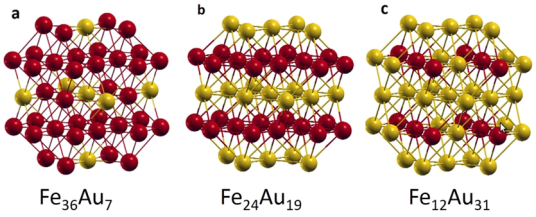

Figure 6. Fe–Au nanoparticle structures used in the density-functional calculations of the magnetic properties: (a) in $L1_2$-ordered Fe_3Au, (b) $L1_0$ FeAu, and (c) Au_3Fe. Each nanoparticle contains 43 atoms, and the structural and compositional data are taken from experiment. Red and yellow spheres indicate Fe and Au atoms, respectively.

contribution of Au to the total magnetization was neglected. Thus, we assumed that the total magnetization arose from only the Fe atoms. The relaxation of atomic coordinates did not change the values of atomic moments beyond the error. Experimentally, the magnetic moment per Fe atom was determined by converting emu per gram to μ_B per Fe atom by normalizing to the approximate number of Fe atoms in a typically sized nanoparticle (the approximate no. of atoms is $\sim 10^4$ for a 5 nm particle). Similarly, the total moment for the entire 43 atom cluster is calculated and then normalized to the number of Fe atoms. In this way, we can more easily compare the calculated magnetic moments with the experimental results on a per Fe atom basis (Table 1).

For $Fe_{36}Au_7$, the calculated average Fe moment is $2.49\mu_B$, which is reasonably close to the experimental value of $2.98\mu_B$. The calculated average Fe moment of $Au_{31}Fe_{12}$ is $0.51\mu_B$ per Fe atom which agrees approximately with experiments (about $0.85\mu_B$). The nonzero magnetic moment is due to uncompensated surface spins for both 43 atom model cluster and nanoparticle. For $Fe_{24}Au_{19}$, which in this case is antiferromagnetic, the calculated average Fe moment is zero because of the lack of uncompensated surface spins in the 43 atom cluster; in the nanoparticle, uncompensated surface spins exist, giving rise to the small net magnetization and nominal magnetic moment of $\sim 0.23\mu_B$ per Fe atom. In all three cases, the calculated and observed magnetic moments are in good agreement, suggesting that the spin structure and atomic structure observed experimentally in each case are correct.

CONCLUSIONS

In summary, we have demonstrated that the nonequilibrium chemically ordered $L1_2$ and $L1_0$ phases are stable phases in Fe–Au nanoparticles. These structures, obtained after heat treatment followed by slow cooling, are effectively products of solid–solid phase transformations and a disorder–order transformation upon cooling. The occurrence of these phases is in contrast to the equilibrium phase diagram. The finite size of the nanoparticles plays a crucial role in the formation of these ordered structures, as the equilibrium phase formation is suppressed by the scale of the system. The enthalpy of formation of the compounds decreases as the particle size decreases, and below a critical size this becomes smaller than the surface energy of the particles. The nanoparticle in this size range can sustain a metastable compound structure. Magnetic ordering of these compounds changes with structure. Ferromagnetic behavior with a high saturation magnetization has been observed in Fe_3Au. The other two compounds (FeAu and $FeAu_3$) show very low saturation magnetization, which cannot be explained by the dilution of Fe with Au. The low magnetization values can be explained by an antiferromagnetically ordered core along with the presence of uncompensated surface spins. The magnetic spin ordering associated with these chemically ordered structures is calculated from first-principle. The calculations predict that ferromagnetic ordering is the energetically most favorable configuration for Fe_3Au. For the $L1_2$ $FeAu_3$ structure, antiferromagnetic ordering is the most stable configuration. The energy difference between ferromagnetic and antiferromagnetic configurations is negligible for FeAu, and stabilization of either spin structure is possible, although experimentally it appears to be AFM. The experimentally observed Fe magnetic moments in these three configurations agree approximately with the theoretical calculations as well.

METHODS

FeAu alloy particles were prepared by inert gas condensation[37] with in a sputtering chamber whose base pressure was kept below 10^{-7} Torr. A mixture of Ar/He gas was used to sputter the target and maintaining temperature balance inside the chamber. The deposition rates were measured *in situ* using a quartz crystal thickness monitor. The atomic gas mixture of Au and Fe was condensed to form particles at −130 °C inside a liquid nitrogen cooled chamber. The as-formed particles were deposited onto a C coated Cu grid for TEM characterization and on a Si substrate for magnetic measurements. Alternate layers of C/SiO_2 and Fe–Au particle layers were deposited to isolate the particles during heat treatment.

The composition of the particles was controlled by using a composite target with different numbers of Au "plugs" inserted into a Fe target. Here, 2, 6, and 8 Au plugs, each 1/4″ in diameter, were inserted around the characteristic "racetrack" typical of magnetron sputtering. From estimates using sputtering rates for both Fe and Au, each plug increases the Au content by approximately 8 atomic percent. Samples are denoted as 2P, 6P, and 8P. For the characterization using transmission electron microscopy (TEM), the particles were deposited directly onto carbon support films and subsequently covered with about 5 nm C or SiO_2 films using a second RF sputtering system available in the system to avoid oxidation. The heat treatment of the nanoparticle samples was performed at 600 °C for 15 min in a quartz capsule filled with ultrahigh purity Ar after repeated evacuations. The samples were furnace-cooled to room temperature.

The structural and compositional characterizations of the nanoparticles were performed using TEM with an FEI Osiris

and Tecnai G^2 F20. The image analysis was carried out using ImageJ. The compositions of the particles were determined by energy dispersive X-ray spectroscopy (EDS) in the transmission electron microscope using a nonconverged electron probe for simultaneous sampling of a large number of particles and standardless analysis.

For the magnetic measurements, the particles were embedded in a C or SiO_2 matrix by alternate deposition from the particle source and the RF source. The total thickness of these composite films was between 30 to 60 nm. The magnetic measurements were conducted at 10 and 300 K using a Quantum Design Magnetic Property Measurement System (MPMS) superconducting quantum interference device (SQUID) magnetometer with a maximum field of 7 T. The magnetic signal from the diamagnetic Si substrate was subtracted from the sample signal by fitting a straight line to the high-field region and subtracting the linear portion from the measured signal. The saturation magnetizations were calculated by plotting M *vs* $1/H^2$ in the high-field regions and extrapolating to $1/H^2 = 0$.

The magnetization was normalized to the number of Fe atoms (n_{Fe}) in the nanoparticles. First of all, nanoparticles were deposited on the TEM grid and the Si substrate (for magnetic measurement) under the same deposition conditions (deposition rate, chamber pressure, gas flow rate, and average film thickness). An individual layer of the multilayer sample for magnetic measurement was identical to the sample on the TEM grid. The size distribution was calculated from the TEM images and from this the average volume of the nanoparticles in a single layer was determined. The saturation magnetization of the sample was then normalized to the overall volume of the nanaoparticles in the multilayer film. As the structure of the nanoparticles were known, the theoretical density and subsequently the mass of the nanoparticles were determined. The number of Fe atoms (n_{Fe}) in a nanoparticle is calculated from the lattice parameter and the nanoparticle volume. The same (n_{Fe}) for a single layer was calculated from the volume distribution. The saturation magnetization was then finally normalized to the number of Fe atoms in a multilayer film.

The first-principle calculations have been performed in the framework of density functional theory (DFT) using projected augmented method (PAW) as implemented in Vienna *ab initio* simulation package (VASP).[38] The exchange-correlation effects were treated using generalized gradient approximation (GGA-PBE). The calculations have been performed using lattice parameters obtained in our experiments. For the bulk calculations, $20 \times 20 \times 10$ Monkhorst−Pack grid for *k*-point sampling is used.[39] For the particles calculations, Γ-point is used for k-point sampling. All the particles are placed in a cubic supercell with 1.5 nm of vacuum to ensure that there is no interaction between neighboring particles. The convergence criterion of 10^{-4} eV has been used for electronic structure. Our experimental results are supported by the DFT simulations.

Conflict of Interest: The authors declare no competing financial interest.

Acknowledgment. P.M. and J.E.S. were supported by the U.S. Department of Energy EPSCoR State and National Laboratory Partnership Program through Grant No. DE-SC0001269. Electron microscopy at Ames Laboratory (L.Z. and M.J.K.) is supported by the U.S. Department of Energy (USDOE), Office of Science (OS), Office of Basic Energy Sciences (BES) under Contract No. DE-AC02-07CH11358. Synthesis and magnetism studies of P.M. and D.S. were supported by USDOE Basic Energy studies, Materials Science and Engineering grant DE-FG02-04ER46152. Theoretical research of Pr.M., P.K., A.K., and R.S. was supported by the US Army Research Office Grant No. WF911NF-10-2-0099. This research was performed in part in Central Facilities of the Nebraska Center for Materials and Nanoscience, which is supported by the Nebraska Research Initiative. Electron microscopy research was supported by NSF-MRI (DMR-0960110).

Supporting Information Available: Detailed calculations of energetics of nanocompound stability and structural characterization of FeAu nanocompounds. This material is available free of charge *via* the Internet at http://pubs.acs.org.

REFERENCES AND NOTES

1. Hills, C. W.; Mack, N. H.; Nuzzo, R. G. The Size-Dependent Structural Phase Behaviors of Supported Bimetallic (PtRu) Nanoparticles. *J. Phys. Chem. B* **2003**, *107*, 2626–2636.
2. Rong, C. B.; D. Li, V. N.; Poudyal, N.; Ding, Y.; Wang, Z.; Zeng, H.; Liu, J. Size-Dependent Chemical and Magnetic Ordering in $L1_0$-FePt Nanoparticles. *Adv. Mater.* **2006**, *18*, 2984–2988.
3. Thompson, D. T. Using Gold Nanoparticles for Catalysis. *Nano Today* **2007**, *2*, 40–43.
4. Zhong, C. J.; Maye, M. M. Core-Shell Assembled Nanoparticles As Catalysts. *Adv. Mater.* **2001**, *13*, 1507.
5. Chiang, I. C.; Chen, D. H. Synthesis of Monodisperse FeAu Nanoparticles with Tunable Magnetic and Optical Properties. *Adv. Funct. Mater.* **2007**, *17*, 1311–1316.
6. Zhou, R.; Wei, X.; He, K.; Shield, J. E.; Sellmyer, D. J.; Zeng, X. C. Theoretical and Experimental Characterization of Structures of MnAu Nanoclusters in the Size Range of 1−3 nm. *ACS Nano* **2011**, *5*, 9966–9976.
7. Mukherjee, P.; Zhou, L.; Kramer, M. J.; Shield, J. E. Formation of Non-Equilibrium Fe-Au Solid Solutions in Nanoclusters. *Appl. Phys. Lett.* **2013**, *102*, 243103.
8. Tabrizi, N. S.; Xu, Q.; van der Pers, N. M.; Schmidt-Ott, A. Generation of Mixed Metallic Nanoparticles from Immiscible Metals by Spark Discharge. *J. Nanoparticle. Res.* **2010**, *12*, 247–259.
9. Peng, Z.; Yang, H. AgPt Alloy Nanoparticles with the Compositions in the Miscibility Gap. *J. Solid State Chem.* **2008**, *181*, 1546–1551.
10. Lee, J. G.; Mori, H.; Yasuda, H. *In-Situ* Observation of a Fluid Amorphous Phase Formed in Isolated Nanometer-Sized Particles in the Sn-Bi System. *Phys. Rev. B* **2002**, *66*, 012105.
11. Perepezko, J. Nucleation-Controlled Reactions and Metastable Structures. *Prog. Mater. Sc.* **2004**, *49*, 268–284.
12. Masalski, T. B. *Binary Alloy Phase Diagram*, 2nd ed.; ASM International: Materials Park, OH, 1990; Vol. 1, pp 367−369.
13. Boscoa, E.; Enzob, S.; Baricoca, M. X-ray Analysis of Microstructure in AuFe Melt Spun Alloys. *J. Magn. Magn. Mater.* **2003**, *262*, 136–141.
14. Mukherjee, P.; Xiang, X.; Wu, Y.; Kramer, M. J.; Shield, J. E. Nucleation Supressed Phase Transformation in FeAu Nanoclusters. *J. Phys. Chem. C* **2013**, *117*, 24071–24078.
15. Golkar, F.; Kramer, M. J.; Zhang, Y.; Skomski, R.; Sellmyer, D. J.; Shield, J. E. Solubility Extension and Phase Formation in Gas-Condensed Co-W Nanoclusters. *J. Nanopart. Res.* **2013**, *15*, 1638.
16. Mukherjee, P.; Zhang, Y.; Kramer, M. J.; Lewis, L. H.; Shield, J. E. $L1_0$ Phase Formation in Slow Cooled Fe-Au Nanoclusters. *Appl. Phys. Lett.* **2012**, *100*, 211911.
17. Apinaniz, E.; Plazaola, F.; Garitaonandia, J. S.; MartÃn, D.; Jimenez, J. A. Study of the Enhancement of the Magnetic Properties of $Fe_{70}Al_{30}$ in the Order-Disorder Transition. *J. Appl. Phys.* **2003**, *93*, 7649–7651.
18. Himuro, Y.; Tanaka, Y.; Kamiya, N.; Ohnuma, I.; Kainuma, R.; Ishida, K. Stability of Ordered $L1_2$ phase in Ni_3Fe-Ni_3x (x: Si and Al) Pseudobinary Alloys. *Intermetallics* **2004**, *12*, 635–643.
19. Alloyeau, D.; Langlois, C.; Ricolleau, C.; Bouar, Y. L.; Loiseau, A. A TEM *in situ* Experiment As a Guideline for the Synthesis of As-Grown Ordered CoPt Nanoparticles. *Nanotechnology* **2007**, *18*, 375301.
20. Qiu, J.; Wang, J. Tuning the Crystal Structure and Magnetic Properties of FePt Nanomagnets. *Adv. Mater.* **2007**, *19*, 1703–1706.
21. Sato, K.; Hirotsu, Y. Structure and Magnetic Property Changes of Epitaxially Grown $L1_0$-FePd Isolated Nanoparticles on Annealing. *J. Appl. Phys.* **2003**, *93*, 6291–6298.
22. Heitsch, A. T.; Lee, D. C.; Korgel, B. A. Antiferromagnetic Single Domain $L1_2$ $FePt_3$ Nanocrystals. *J. Phys. Chem. C* **2010**, *114*, 2512–2518.
23. Ko, H. Y.; Suzuki, T.; Nam, N. T.; Phuoc, N. N.; Cao, J.; Hirotsu, Y. Magnetic and Structural Characterizations on Nanoparticles of FePt, FeRh and Their Composites. *J. Magn. Magn. Mater.* **2008**, *320*, 3120–3123.

24. Bondi, J. F.; Misra, R.; Ke, X.; Sines, I. T.; Schiffer, P.; Schaak, R. E. Optimized Synthesis and Magnetic Properties of Intermetallic Au_3Fe_{1-x}, Au_3Co_{1-x}, and Au_3Ni_{1-x} Nanoparticles. *Chem. Mater.* **2010**, *22*, 3988–3994.
25. Vasquez, Y.; Luo, Z.; Schaak, R. E. Low-Temperature Solution Synthesis of the Non-Equilibrium Ordered Intermetallic Compounds Au_3Fe, Au_3Co, and Au_3Ni As Nanocrystals. *J. Am. Chem. Soc.* **2008**, *130*, 11866–11867.
26. Lee, K. W.; Lee, Y. J.; Han, D. S. The Log-Normal Size Distribution Theory for Brownian Coagulation in the Low Knudsen Number Regime. *J. Colloid Interface Sc.* **1997**, *188*, 486–492.
27. Luo, Z.; Vasquez, Y.; Bondi, J.; Schaak, R. Pawley and Rietveld Refinements Using Electron Diffraction from $L1_2$-type Intermetallic Au_3Fe_{1-x} Nanocrystals During Their *in-Situ* Order-Disorder Transition. *Ultramicroscopy* **2011**, *111*, 1295–1304.
28. Liang, L. H.; Yang, G. W.; Li, B. Size-Dependent Formation Enthalpy of Nanocompounds. *J. Phys. Chem. B* **2005**, *109*, 16081–16083.
29. de Boer, F.; Boom, R.; Mattens, W. M.; Niessen, A. *Cohesion in Metals*, 1st ed.; North-Holland: Amsterdam, 1988; Vol. 1, p 224.
30. Himpsel, F. J.; Ortega, J. E.; Mankey, G. J.; Willis, R. F. Magnetic Nanostructures. *Adv. Phys.* **1998**, *47*, 511–597.
31. Nanda, K. K.; Maisels, A.; Kruis, F. E.; Fissan, H.; Stappert, S. Higher Surface Energy of Free Nanoparticles. *Phys. Rev. Lett.* **2003**, *91*, 106102.
32. van Giessen, A. E.; Blokhuis, E. M.; Bukman, D. J. Mean Field Curvature Corrections to the Surface Tension. *J. Chem. Phys.* **1998**, *108*, 1148.
33. Kuznetsov, V. M.; Kadyrov, R. I.; Rudenskii, G. E. Calculation of Surface Energy of Metals and Alloys by the Electron Density Functional Method. *J. Mater. Sci. Tech.* **1998**, *14*, 320–322.
34. Dannenberg, A.; Gruner, M. E.; Hucht, A.; Entel, P. Surface Energies of Stoichiometric FePt and CoPt Alloys and their Implications for Nanoparticle Morphologies. *Phys. Rev. B* **2009**, *80*, 245438.
35. Morales, M. A.; Skomski, R.; Fritz, S.; Shelburne, G.; Shield, J. E.; Yin, M.; O'Brien, S.; Leslie-Pelecky, D. L. Surface Anisotropy and Magnetic Freezing of MnO Nanoparticles. *Phys. Rev. B* **2007**, *75*, 134423.
36. Panaccione, G.; Sirotti, F.; Rossi, G. Surface vs. Bulk Magnetic Moments from Photoemission Dichroism. *Solid. State Commun.* **2000**, *113*, 373–377.
37. Haberland, H.; Karrais, M.; Mall, M.; Thurner, Y. Thin Films from Energetic Cluster Impact: A Feasibility Study. *J. Vac. Sc. Technol.* **1992**, *A10*, 3266–3271.
38. Kresse, G.; Joubert, D. From Ultrasoft Pseudopotential to the Projected Augmented-Wave Method. *Phys. Rev. B* **1999**, *59*, 1758.
39. Monkhorst, H. J.; Pack, J. D. Special Points for Brillouin-Zone Integrations. *Phys. Rev. B* **1976**, *13*, 5188.